

Underwater Image Enhancement Method via Multi-Interval Subhistogram Perspective Equalization

Jingchun Zhou¹, Lei Pang¹, Dehuan Zhang, and Weishi Zhang¹

Abstract—Due to the selective attenuation of light in water, captured underwater images exhibit poor visibility and cause considerable challenges for vision tasks. The structural and statistical properties of different regions of degraded underwater images are damaged at different levels, resulting in a global nonuniform drift of the feature representation, causing further degradation of visual performance. To handle these issues, we present an underwater image enhancement method via multi-interval subhistogram perspective equalization to address the issues posed by underwater images. We estimate the degree of feature drifts in each area of an image by extracting the statistical characteristics of the image, using this information to guide feature enhancement to achieve adaptive feature enhancement, thereby improving the visual effect of degraded images. We first design a variational model that uses the difference between data items and regular items to improve the color correction performance of the method based on subinterval linear transformation. In addition, a multithreshold selection method, which adaptively selects a threshold array for interval division, is developed. Ultimately, a multi-interval subhistogram equalization method, which performs histogram equalization in each subhistogram to improve the image contrast, is presented. Experiments on underwater images with various scenarios demonstrate that our method significantly outperforms many state-of-the-art methods qualitatively and quantitatively.

Index Terms—Multiple intervals, multiscale fusion (MF), subhistogram equalization (SHE), underwater image.

I. INTRODUCTION

HIGH-QUALITY visual information is crucial in many activities, such as underwater welding and seabed exploration, but the complex underwater environment makes obtaining clear underwater images difficult [1]. The structure and statistical properties of different regions of an acquired degraded underwater image damage at different levels are due

Manuscript received 24 May 2022; revised 12 October 2022; accepted 14 November 2022. Date of publication 7 February 2023; date of current version 14 April 2023. This work was supported in part by the National Natural Science Foundation of China under Grant 61702074, in part by the Liaoning Provincial Natural Science Foundation of China under Grant 20170520196, and in part by the Fundamental Research Funds for the Central Universities under Grant 3132019205 and Grant 3132019354. (*Corresponding authors:* Weishi Zhang, Jingchun Zhou.)

Associate Editor: H. Zheng.

The authors are with the College of Information Science and Technology, Dalian Maritime University, Dalian 116026, China (e-mail: zhouchingchun03@qq.com; boss19980411@dlnu.edu.cn; zhangdehuan@dlnu.edu.cn; teesiv@dlnu.edu.cn).

Digital Object Identifier 10.1109/JOE.2022.3223733

to selective attenuation based on the light wavelength, which results in a global nonuniform drift of the feature representation and further leads to the low contrast and visibility of underwater images; hence, some enhancements are required for meaningful information to be extracted from them [2], [3]. Many enhancement methods have been proposed to enhance the quality of underwater images [4], [5], [6], [7], [8]. Nevertheless, most of them ignore the importance of extracting statistical features of images, which leads to distortion effects in the output images. Thus, available mature vision algorithms face significant challenges in achieving the expected performance for underwater image enhancement.

Various methods have been proposed to solve underwater image degradation. One commonly used method is histogram equalization (HE), which has the advantages of simple calculation and easy implementation. However, HE also has issues. For example, it decreases information entropy (IE) and blurs details in an image. Given these shortcomings, some representative improvements have been proposed, one of which is the subhistogram equalization (SHE) method [9], [10], [11], [12], [13], [14], [15], [16]. The SHE method has better image enhancement performance than HE. For example, brightness preserving bihistogram equalization [17] divides a histogram into two subhistograms, and HE is performed on each equal area. The dualistic subimage HE method [18] was proposed based on SHE and used the original probability density function to divide a histogram. Furthermore, Khan et al. [19] proposed a fuzzy double HE method that uses the skewness of the histogram to obtain the segmentation threshold. However, these methods do not significantly enhance underwater images because they ignore the characteristics of underwater image histograms. An image's histogram is usually adopted to describe the statistical distribution of the image's color. The degradation of underwater images has a severe impact on the histogram. Therefore, the histograms of underwater images should be analyzed by subjective evaluation to solve underwater image degradation. Fig. 1 shows some representative underwater images, their corresponding polyline and 3-D histograms, and their gradient frequency histograms. Polyline histograms visually display the trend and distribution of the histogram, whereas 3-D histograms better show the image's color distribution. By observing both types of histograms, the following three critical features of underwater images are revealed.

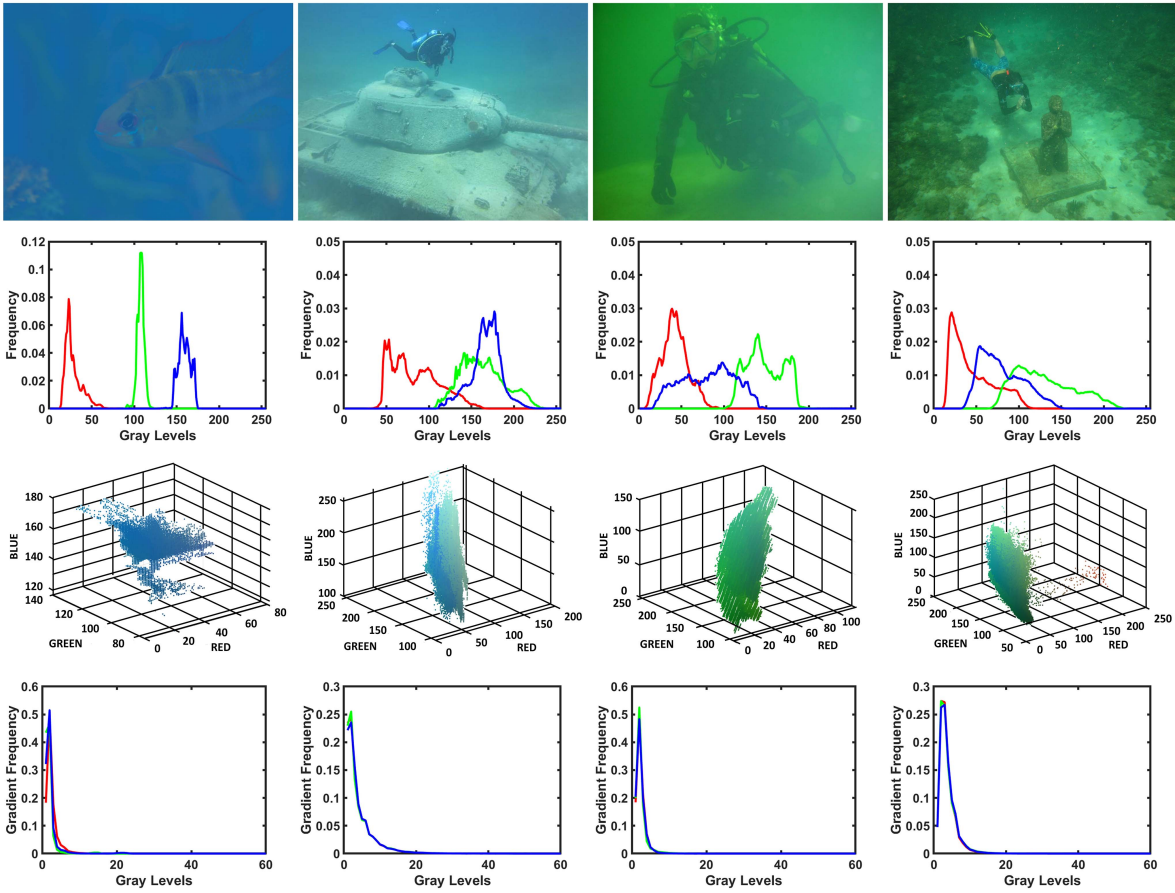


Fig. 1. Some representative underwater images and their corresponding polyline, 3-D, and gradient frequency histograms. From top to bottom are the original underwater images, the polyline histograms, 3-D histograms, and the gradient frequency histograms.

- 1) *Uneven distribution:* In Fig. 1, the polyline histograms have characteristics of imbalance and instability (i.e., the polyline histograms are scattered to both sides or concentrated in the middle). The 3-D histograms contain scattered pixels due to the color cast.
- 2) *Concentration:* The polyline histograms show that the histogram pixels of the underwater images are concentrated in a relatively narrow area. The maximum pixel frequency is usually found in this area.
- 3) *Deviation:* The polyline histograms show that pixels corresponding to the deviated color of the underwater images are usually concentrated in high-pixel areas. The greater the color deviation is, the greater the color's pixel frequency in the high-pixel area.

In addition, the gradient frequency histograms of the underwater images have the characteristics of a left-skewed distribution. Because underwater images are affected by light absorption, scattering, and underwater plankton, their histograms usually have uneven distributions, concentrations, and deviations. These characteristics subsequently affect the quality of the underwater imaging process, resulting in the final degraded images.

This study proposes a novel underwater image enhancement method via multi-interval subhistogram perspective equalization (UMSHE) to adjust the histogram of underwater images. The main contributions of this study are summarized as follows.

- 1) We present a color correction method based on a subinterval linear transformation and a variational model (SLVC). The enhanced method removes the color cast and improves color saturation to imitate human visual effects.
- 2) We propose a novel method of threshold selection. This method adaptively selects a threshold array and divides the histogram into multiple intervals to obtain multiple subhistograms.
- 3) We design a multi-interval SHE method. This method extends the SHE method of fixed intervals to multiple intervals. It can adaptively equalize each subinterval according to the number of intervals, improving the method's adaptability.

II. RELATED WORK

Existing underwater vision enhancement techniques can be classified into three categories: underwater image restoration, underwater image enhancement, and deep learning-based methods.

A. Underwater Image Restoration Methods

Underwater image restoration methods aim to establish an effective underwater image degradation model to restore image quality [20]. Common underwater image restoration methods

include polarization characteristics-based methods [21], [22], [23]; underwater optical imaging-based methods [24], [25], [26]; and methods based on prior knowledge [27], [28], [29], [30], [31]. Treibitz and Schechner [21] estimated the degree of polarization of the background light in two or more images of the same scene. Chen et al. [22] proposed a region-specific estimation method and used the dark channel prior (DCP) to estimate the region's haze concentration and depth map. Hu et al. [23] restored underwater images based on transmittance correction by changing the transmittance of low polarization. Trucco and Antillon [24] proposed a simplified Jaffe-McGlamery underwater optical image model based on the assumption that underwater images are affected by uniform illumination and forward scattering. Hou et al. [25] restored images by incorporating underwater optical characteristics into the system response function. Boffety et al. [26] investigated the impact of the spectral discretization of model parameters on the color rendering of an image. The DCP method proposed by He et al. [27] is the most used in image defogging, and DCP-based deblurring methods are also widely used in underwater image enhancement. Drews et al. [28] proposed a dark underwater channel prior (UDCP) method, which only considers the green-blue (G, B) channel to eliminate the influence of the red (R) channel. Peng and Cosman [29] produced a more accurate background light estimation with image blurring and light absorption (IBLA). Li et al. [30] restored images based on the minimum information loss principle and used histogram distribution priors. Song et al. [31] obtained a scene depth map and estimated the background light using a linear model. Even though most restoration methods can solve some underwater image degradation problems, their performance is limited due to inaccurate estimation of essential model parameters and ignoring the influence of backscattering on optical imaging.

B. Underwater Image Enhancement Methods

Underwater image enhancement methods enhance images by adjusting pixel intensity distribution. Commonly used methods for underwater images can be grouped into spatial domain methods [32], [33], [34], transform domain methods [35], [36], [37], and fusion-based methods [38], [39], [40]. Iqbal et al. [32] stretched the attenuated G B channel in the RGB color model and the saturation (S) components in the Hue to enhance the images. Fu et al. [33] proposed a two-step approach for single underwater image enhancement (TS) that solved two subproblems to enhance underwater images. Huang et al. [34] proposed relative global histogram stretching (RGHS) in the RGB and CIE-Lab color models. Amjad et al. [35] addressed low contrast and color change issues using a wavelet-based fusion method. Liu et al. [36] proposed an effective multiscale correlation wavelet method (WB) to solve frequency domain image dehazing problems. Vasamsetti et al. [37] proposed a wavelet-based perspective enhancement framework for underwater images. Ancuti et al. [38] recently obtained fusion weight maps from degraded underwater images. Then, Ancuti et al. [39] made further improvements to the fusion method by applying the traditional methods to raw images. Lu et al. [40] improved underwater images by fusing

the images denoised by the scattering method and the results from the self-exemplary superresolution method. Underwater image enhancement methods are designed for a specific task but ignore the attenuation factor. The same processing technique is used for all scene images, resulting in overenhancement or underenhancement. These methods rarely consider the structural and statistical properties of underwater images, which should be paid more attention to in the future.

C. Deep Learning Based Methods

Deep learning technologies have been introduced to low-level tasks. Based on the network architecture, recent deep learning methods applied to underwater images can be divided into dual generator generative adversarial networks (GANs) [41], [42], multibranch designs [43], [44], depth-guided networks [45], and prior-based networks [46]. Li et al. [41] proposed a supervised algorithm for underwater image color correction based on GAN [42] called UWGAN, which has a cyclic structure that includes a forward and backward network to extract the unique characteristics of the image set. Furthermore, Li et al. [43] proposed a gated fusion convolutional neural network (CNN) method trained on an underwater imaging improvement database they constructed. The fusion generative confrontation network [44] can accept multiple inputs, which can be passed through different paths in the network. Cao et al. [45] proposed a deep network for image restoration based on classic restoration methods. Li et al. [46] proposed a CNN model that uses prior knowledge to generate underwater image training data and provides sufficient training data for lightweight networks. However, the application scope of these techniques is still limited because the performance of deep learning-assisted methods depends on the network structure design and training data.

III. METHOD

Based on the structural and statistical properties of underwater images, an underwater image enhancement method via multi-interval subhistogram perspective equalization is proposed to address the issues posed by underwater images. The proposed method consists of color correction, contrast enhancement, and multiscale fusion (MF). The flow chart of the detailed steps of the proposed method (see Fig. 2) is divided into three corresponding subgraphs. The various parts of the proposed method are described in detail as follows.

A. Color Correction

To solve the color cast and enhance the saturation of underwater images, the proposed method designs a color correction method based on an SLVC. This method directly processes the pixels, removes the color cast by linearly stretching and transforming the pixels, and establishes the competitive relationship between the regular item and the data item of the variational model. Finally, SLVC can improve the image color saturation and correct the color effectively. Additionally, this method is easy to implement and can enhance the image's highlight details. The main steps of the process are as follows.

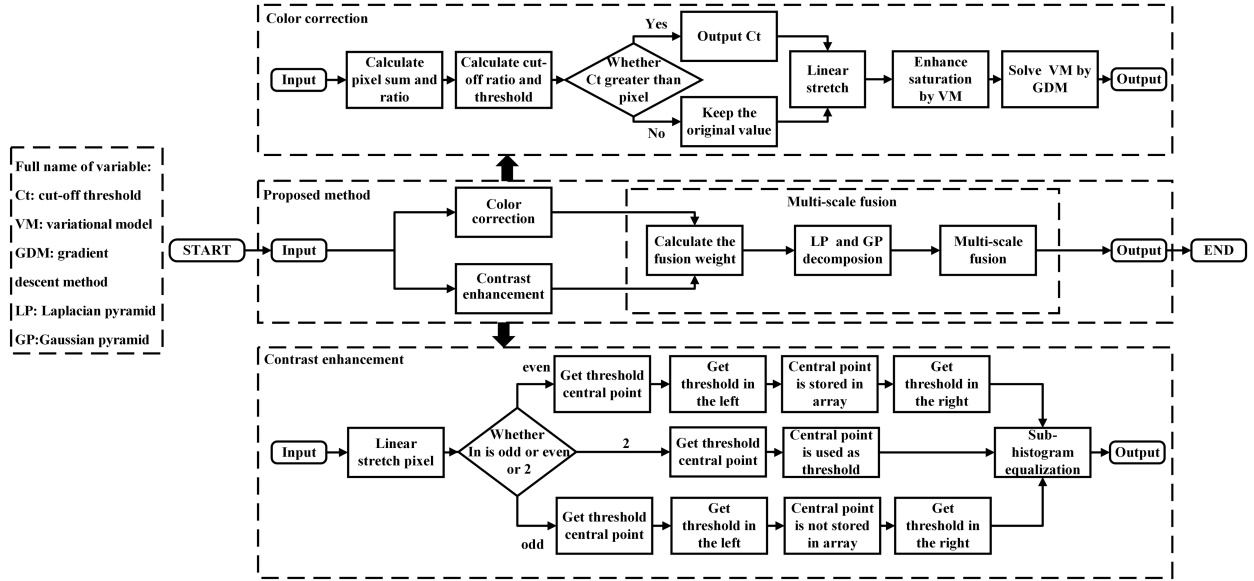


Fig. 2. Flowchart of the detailed steps of the proposed method, which consists of three subflows: color correction, contrast enhancement, and MF.

First, the single-channel pixel sum is calculated using

$$S_c = \sum_{i=1}^{P \times Q} I_c(t) \quad (1)$$

where I is the input image, t is the pixel gray level, c denotes the three channels of the RGB image, $I_c(t)$ refers to the pixel value in the channel c , P refers to the number of rows of the matrix transformed by the input image, Q represents the number of columns, and S_c denotes the total pixel number of a specific channel c .

Then, the ratio of the maximum total pixels of each channel to the total pixel of that channel is calculated as follows:

$$R_c = \frac{\text{Max}\{S_R, S_G, S_B\}}{S_c} \quad (2)$$

where Max is the maximum value function, and R_c denotes the ratio of the maximum total pixels to the total pixels of the specific channel c .

Then, two cutoff ratios are used to calculate the cutoff thresholds and divide the channel into three parts. The cutoff ratios are calculated using the following equations:

$$\varpi_1^c = \theta_1 \times R_c \quad (3)$$

$$\varpi_2^c = \theta_2 \times R_c \quad (4)$$

where ϖ_1^c and ϖ_2^c represent the cutoff ratios, and θ_1 and θ_2 are two constants in $(0,1)$. According to [47] and the extensive experimental verification, the values of θ_1 and θ_2 are 0.001 and 0.005, respectively.

Next, the cutoff thresholds that are used for the linear transformation are determined using the lower quantile function as follows:

$$e_1^c = F(I_c(t), \varpi_1^c) \quad (5)$$

$$e_2^c = F(I_c(t), \varpi_2^c) \quad (6)$$

where e_1^c and e_2^c represent the cutoff thresholds, and F is the lower quantile function.

The pixel values replaced by the first cutoff threshold are less than the value of the first cutoff threshold, whereas the second cutoff threshold returns pixel values more significant than the value of the second cutoff threshold. The cutoff thresholds and pixel values are calculated as follows:

$$I_e^c(t) = \begin{cases} e_1^c & I_c(t) < e_1^c \\ e_2^c & I_c(t) > e_2^c \end{cases} \quad (7)$$

where $I_e^c(t)$ refers to the postprocessing pixel value.

Then, the pixel values are stretched linearly using

$$I_S^c(t) = \frac{I_e^c(t) - e_1^c}{e_2^c - e_1^c} \times 255 \quad (8)$$

where $I_S^c(t)$ denotes a pixel value that has been stretched.

Ultimately, inspired by [48], a variational model with a data term and regularized terms are designed to improve saturation. The data term prevents the resulting image from departing from the restored color by penalizing the difference between μ and $I_S^c(t)$. The regularized terms enhance the saturation by expanding the difference among the R, G, and B components as

$$E(\mu_c) = \frac{1}{2} \sum_t \left(\frac{\mu_c(t) - }{I_S^c(t)} \right)^2 - \frac{\alpha}{2} \sum_t \left(\frac{(\mu_c(t) - \mu_{c+1}(t))^2 + (\mu_c(t) - \mu_{c+2}(t))^2}{+ (\mu_c(t) - \mu_{c+1}(t))^2} \right) \quad (9)$$

where μ_c denotes the enhanced image; c represents a 3-D space of the color image's three channels, including the R, G, and B channels (i.e., $R : c = 1$, $G : c = 2$, and $B : c = 3$); and α is a positive parameter used to control the regular term.

Data and regular items are designed to adjust the contrast and saturation of the image by constructing a competitive relationship [49]. When the competitive relationship between a data item

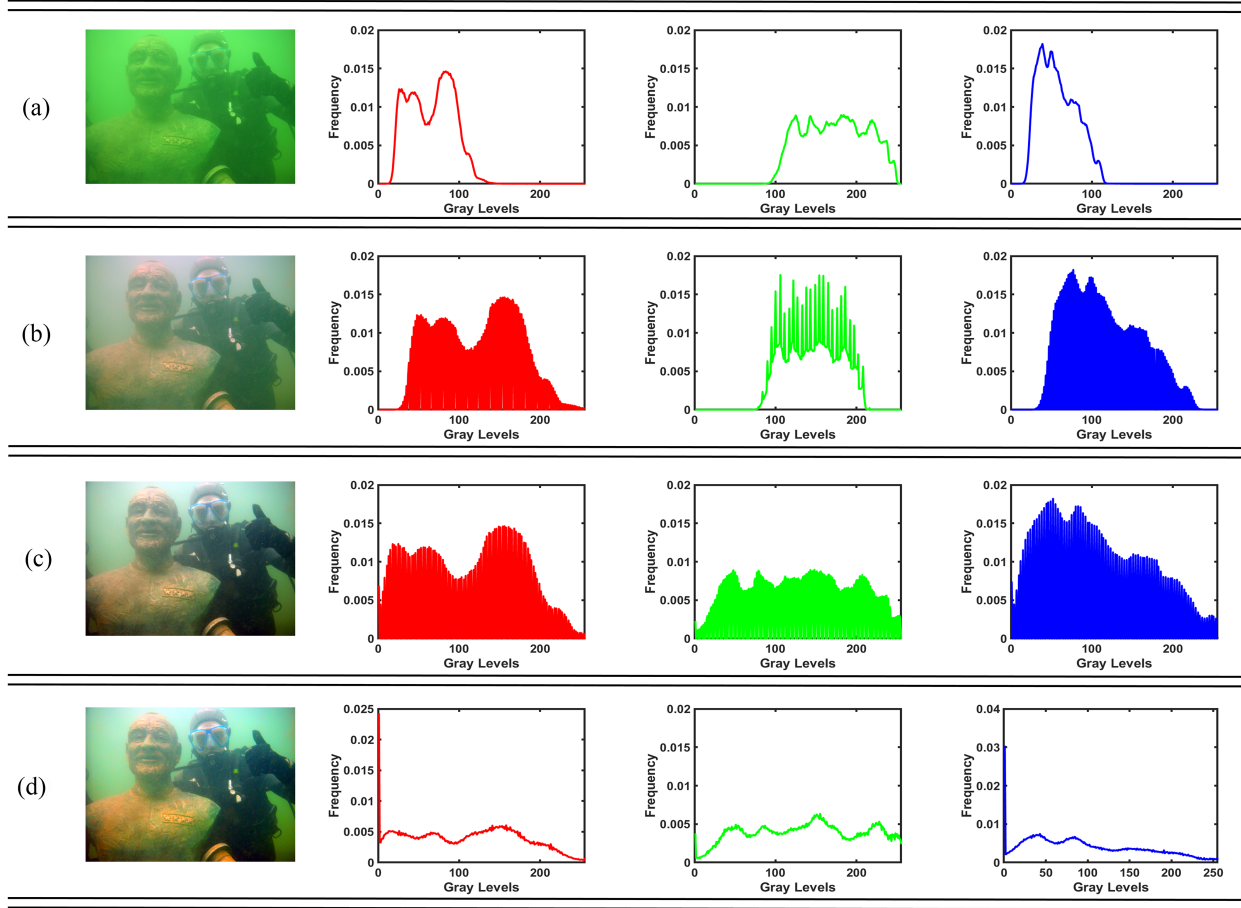


Fig. 3. Comparison of different color correction method results and their corresponding three-channel histograms. From top to bottom, (a) raw image, (b) AWB, (c) SLC, and (d) SLVC. From left to right, subjective results and the histograms of the result of the R, G, and B channels.

and a regular item reaches a state of energy minimization, the contrast and saturation are relatively in line with those obtained by human visual effects.

The gradient descent method is used for the iterative calculation results to perform the minimization operation. The Euler–Lagrange derivative of the model is calculated, as follows:

$$\delta E(\mu_c) = (\mu_c(t) - I_S^c(t)) - \alpha(2\mu_c - \mu_{c+1} - \mu_{c+2}) = 0. \quad (10)$$

Then, the gradient descent strategy is used to solve (10). Starting from the linearly stretched image, (11) is solved as follows:

$$\frac{\partial \mu}{\partial m} = -\delta E(u) \quad (11)$$

where m denotes the timeline of iterative calculations.

Then, (11) is discretized and rewritten as follows:

$$\frac{\mu_c^{k+1}(t) - \mu_c^k(t)}{\Delta m} = \left(\begin{array}{l} I_S^c(t) - \\ \mu_c^k(t) \end{array} \right) + \alpha \left(\begin{array}{l} 2\mu_c^k(t) - \mu_{c+1}^k(t) \\ -\mu_{c+2}^k(t) \end{array} \right) \quad (12)$$

where k denotes the number of iteration calculations. After a simple left-right identity transformation of (12), the iteration

rule is obtained as follows:

$$\begin{aligned} \mu_c^{k+1} &= \mu_c^k (1 - \Delta m (1 - 2\alpha)) \\ &+ \Delta m (I_S^c - \alpha \mu_{c+1}^k - \alpha \mu_{c+2}^k) \end{aligned} \quad (13)$$

where $0 < \Delta m \leq 1/(1 - 2\alpha)$.

Two-color correction methods are selected to compare and analyze the performance of the SLVC method, including the white balance (AWB) method and the subinterval linear transformation (SLC) method. By comparing the subjective results of several methods and the corresponding three-channel histograms in Fig. 3, it can be found that the SLVC method has better color correction effects, and the histogram performs steadily.

B. Contrast Enhancement

An underwater image's level of contrast significantly impacts the image's quality and details. Although the SLVC algorithm solves the issues of color casting and saturation degradation, problems with low contrast and blurred details still exist. Therefore, this study proposes an MSHE method to solve the low contrast and blurry details of underwater images.

The MSHE method divides a histogram into multiple subhistograms and performs HE. By dividing and processing multiple

subhistograms, the histogram correction is better, and the HE is more efficient. Additionally, the MSHE method enhances the image contrast without artifacts and noise. The main steps of the MSHE method are as follows.

Step 1. Pixel stretching: The input underwater images must be preprocessed due to their diversity and pixel sizes. Thus, the following linear stretching operation is performed to ensure that the pixel values are all within [0, 255]:

$$H_c(x) = \frac{(I_c(t) - m_{i_c})}{(m_{a_c} - m_{i_c})} \times 255 \quad (14)$$

where $I_c(t)$ represents the pixel value of the initial image at a certain point; m_{a_c} and m_{i_c} indicate the maximum and minimum pixel values of a single channel image, respectively, and $H_c(t)$ denotes the pixel value after linear stretching.

Step 2. Interval division threshold selection: To adopt the MSHE method, the interval division thresholds must be determined to divide the histogram into multiple subhistograms. First, a central threshold point (C_p) in the entire histogram is determined using the lower quantile method [50]. Then, multiple thresholds are selected around the C_p for interval division.

The criterion for selecting C_p is the statistically lower quantile, within [0.75, 0.8]. This criterion fully considers the characteristics of the left-skewed distribution of the image gradient frequency histogram. The objective law of the image gradient is that the proportion of the slight gradient value is significant, and that of the considerable gradient value is small. If the value of the cumulative distribution function is in [0.75, 0.8], this part of the interval can represent the interval of a small gradient value. The remaining interval in [0.2, 0.25] can represent the interval of the considerable gradient value so that the entire gradient field can be reasonably divided into a small gradient interval and a large gradient interval. However, for many images, the gradient frequency cannot be specified by a uniform value. However, as a statistical percentage, the value in [0.75, 0.8] can completely represent the majority, and the value in [0.25, 0.2] can completely represent the minority. Because of the left-bias characteristics of the gradient frequency histogram, the low-gradient frequency pixels occupy the majority. Therefore, the lower quantile limit uses 0.75 to divide the gradient image into large and small gradient parts. The large gradient part needs to be equalized because it contains too few pixels, and the small gradient part needs to be equalized because it contains too many pixels. Therefore, the value obtained by the lower quantile method is used as C_p to divide the image histogram into two parts that must be adjusted the most.

According to [50], image processing performance is optimal when the threshold is selected on both sides of the central point. Many experiments also demonstrate that this threshold selection is suitable. The threshold selection on both sides of C_p is based on the number of input intervals (N_i) divided into three categories: an odd N_i , an even N_i , and two intervals. Only one interval division threshold is needed when two intervals exist, and the selected C_p is used as the required interval division threshold. After experimental verification, when the threshold selection method on both sides of C_p is consistent, the MSHE

method has the best performance. Due to space limitations, the experiment is shown in the revised list.

When N_i is even, an odd number of interval thresholds is needed. Therefore, C_p is one of the thresholds, and the number of threshold selection operations is calculated according to N_i . Performing a threshold selection operation means two thresholds are selected on the left and right. Then, C_p is used to subtract or add the product of b times the pixel value variance, and the number of times the threshold operation is used to calculate all thresholds. The first item of the interval division threshold array is set to 0, while the last item is set to 256.

When N_i is odd, an even number of interval thresholds is needed. Therefore, C_p is not used as one of the thresholds but only for calculating the other thresholds. The threshold operation is selected according to N_i . The threshold calculation method on both sides of C_p is the same as when N_i is even.

A schematic diagram of the threshold selection method is shown in Fig. 4, where C_p represents the central point, N_i denotes the number of thresholds, d indicates the threshold, and n indicates the number of intervals (i.e., N_i is to the left of C_p when N_i is even and N_i is to the left of C_p when it is odd).

To select C_p , the number and frequency of the occurrence of each pixel value in the input image are calculated as follows:

$$N = \text{imhist}(H_c(t)) \quad (15)$$

$$h = \frac{N}{P \times Q} \quad (16)$$

where $H_c(t)$ denotes the images that have been stretched linearly; imhist represents the function used to count the number of occurrences of pixels; N represents the number of each pixel value in the input image; P and Q represent the number of rows and columns of the matrix from the input image, respectively; and h represents the frequency of the occurrence of each pixel value in the input image.

The frequency of the occurrence of a pixel value is then aggregated until the frequency sum exceeds the set lower quantile as follows:

$$Fs = Fs + h(Cp) \quad (17)$$

where $Fs < Flag$ (Fs denotes the sum of the frequency of occurrence of pixel values), $h(Cp)$ represents the frequency of occurrence of pixel values, and Cp is a positive integer that is used to represent C_p . Based on statistical analysis and experimental validations, the value of $Flag$ is set to 0.75.

The number of required division intervals is then divided into the three previously mentioned categories: two intervals, an odd N_i , and an even N_i . When N_i is 2, C_p is used as the threshold. When N_i is even, the first element of the threshold array is set to 0. Then, the number of times the threshold selection operation (NOTS) is calculated as follows:

$$ce = \text{fix}\left(\frac{n-1}{2}\right) \quad (18)$$

where ce represents the NOTS that had to be performed, fix denotes the round-down function, and n refers to N_i .

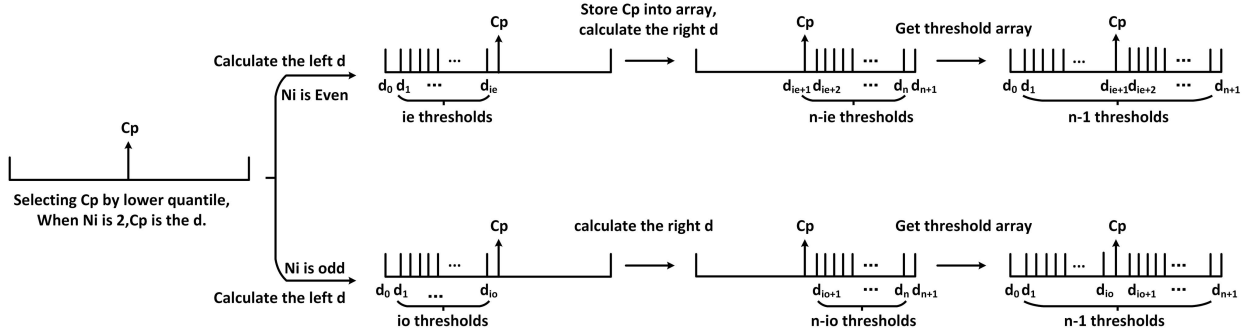


Fig. 4. Schematic diagram of the threshold selection method.

The number of thresholds to the left of Cp is then calculated using

$$ie = \text{ceil} \left(\frac{n-1}{2} \right) \quad (19)$$

where ie represents the number of thresholds to the left of Cp, and ceil denotes the round-up function.

Next, the threshold value on the left side of Cp is calculated using Cp minus b times the product of the pixel value variance, and the NOTS is performed. The NOTS is performed decreased along with the loop calculation. The equations are as follows:

$$d(i) = Cp - b \times ce \times \sigma i \in \{2, ie\} \quad (20)$$

where $d(i)$ represents the i th threshold, which is stored in the threshold array, b is a positive parameter used to find the threshold, and σ refers to the pixel variance in the input image.

After calculating the thresholds on the left side, Cp is stored in the array as one of the thresholds. Then, the thresholds to the right side of Cp are calculated using Cp plus b times the product of the pixel value variance, and the NOTS is performed. The NOTS is performed increases along with the loop calculation. The equations are as follows:

$$d(i) = Cp + b \times je \times \sigma i \in \{ie+2, n\} \quad (21)$$

where je denotes the NOTS is performed.

Next, the last element of the threshold array is set to 256. When the Ni is odd, the first element of the threshold array is also set to 0. Then, the NOTS is calculated, as follows:

$$co = \text{fix} \left(\frac{n}{2} \right) \quad (22)$$

where co represents the NOTS is performed. Afterward, the number of thresholds on the left side of Cp is calculated using

$$io = \frac{n-1}{2} + 1 \quad (23)$$

where io represents the number of thresholds to the left of Cp is performed. Then, the threshold value on the left side of Cp is calculated using Cp minus b times the product of the pixel value variance and the NOTS. The NOTS performed decreased along with the loop calculation. The equation is as follows:

$$d(i) = Cp - b \times co \times \sigma i \in \{2, io\}. \quad (24)$$

Then, the thresholds on the right of Cp are calculated using Cp plus b times the product of the pixel value variance, and NOTS is performed. The NOTS performed increases along with the loop calculation. The equation is as follows:

$$d(i) = Cp + b \times jo \times \sigma i \in \{io+1, n\} \quad (25)$$

where jo denotes the NOTS is performed when Ni is odd. Next, the last element of the threshold array is set to 256.

Step 3. SHE: The histogram is divided into n intervals through the selected $n-1$ thresholds. The histogram between two adjacent thresholds is used as a subhistogram. For example, the histogram between $d(1)$ and $d(2)$ is called subhistogram X_1 , and the histogram between $d(n-1)$ and $d(n)$ is called subhistogram X_n . Then, n subhistograms are obtained, and are represented by $X_1 \sim X_n$. Fig. 5 shows a schematic diagram of the division of the multiple subhistograms and the changes in the histograms before and after the HE.

Then HE is performed on each subhistogram. First, the number of pixels of the subhistogram is calculated using

$$N(a, t) = \text{imhist}(H_c(t)) \quad t \in \{d(a), d(a+1)-1\} \quad (26)$$

where $N(a, t)$ represents the number of pixels of the t th gray level in the a th interval and imhist denotes the function used to calculate the number of pixels in a specific gray level of an image.

The normalized pixel frequency is calculated using the following equations:

$$P(a, t) = \frac{N(a, t)}{S_a} \quad (27)$$

$$CDF(a, t) = \sum_{j=0}^t P(a, t) \quad (28)$$

where $P(a, t)$ represents the t th gray-level pixel frequency in the a th interval, S_a denotes the total number of pixels in the a th interval, and $CDF(a, t)$ represents the t th gray-level cumulative pixel frequency in the a th interval.

Finally, the transformed pixel value of the multiple subhistograms after equalization is obtained using the frequency of the cumulative pixel as follows:

$$y(a, t) = d(a+1) + 1 + (d(a+1) - d(a)) \times CDF(a, t)$$

$$a \in \{1, n\} \quad t \in \{d(a), d(a+1)-1\} \quad (29)$$

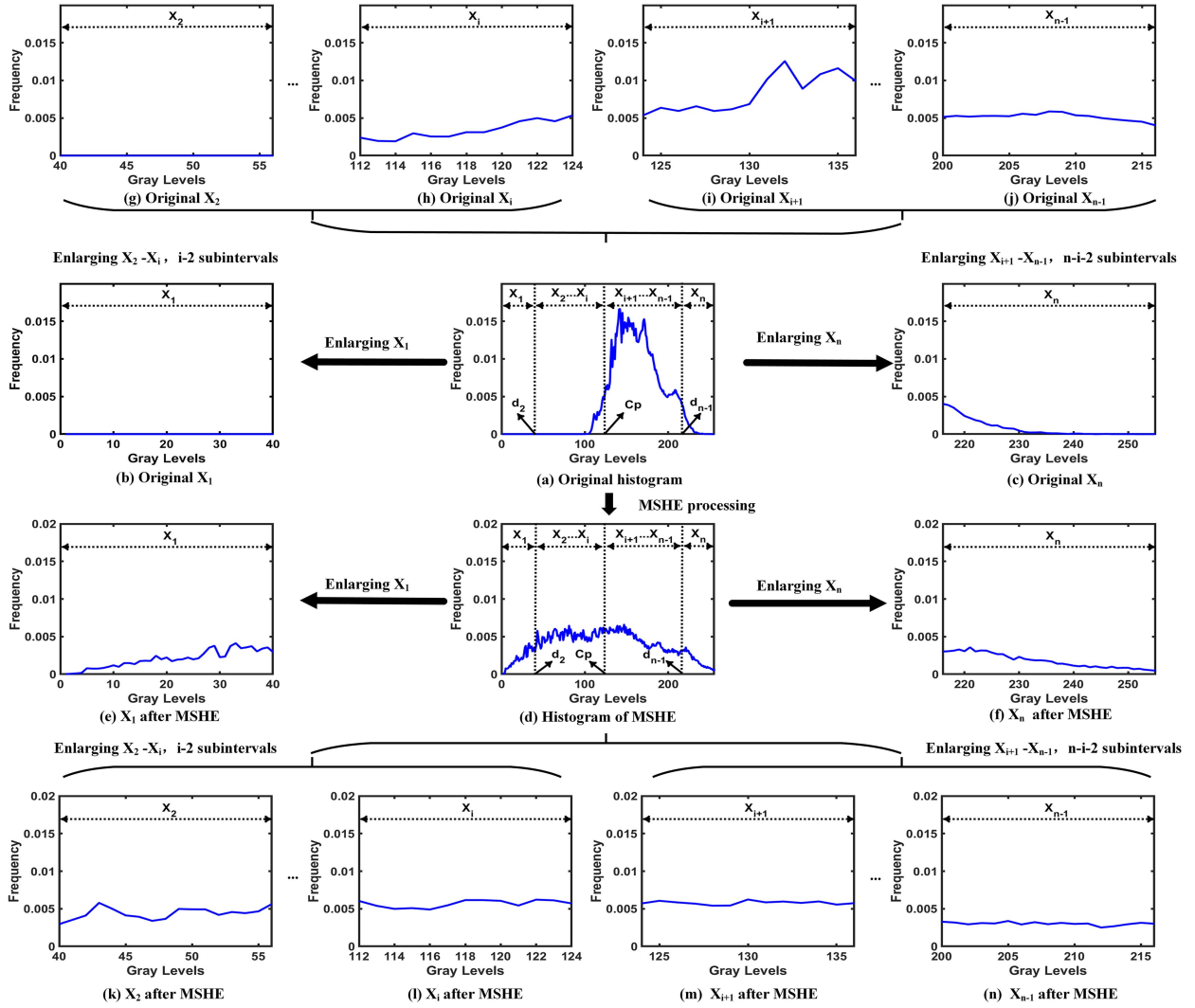


Fig. 5. Schematic diagram of the division of multisubhistograms and the changes before and after the HE. (a) Original histogram division. (b), (c), (g), (h), (i), and (j) Representative original subhistogram. (d) Histogram division processed by MSHE. (e), (f), (k), (l), (m), and (n) corresponding representative subhistograms processed by MSHE.

where $y(a, t)$ denotes the pixel value in the a th interval after HE.

C. Multiscale Fusion

MF [51] is applied to fuse the color correction and contrast enhancement results, which characterize each area in the resulting image by obtaining the best appearance from the input sequence. Although most image enhancement methods have certain limitations, MF based on weight map features can select appropriate pixels from each input image and blend them into a final image.

An essential advantage of MF is the reliably to perform underwater image enhancement through multiscale strategies, even if the distance map is not estimated in advance. Moreover, the results obtained by the enhancement method can be well preserved.

1) *Weight Map*: For each input, the contrast weight, exposure weight, and saturation weight of each image are calculated, and the calculated weight maps are merged into an aggregated weight map. Then, the aggregated weight is normalized by the sum of

the weights of the same pixels in all the images as follows:

$$W = F_C \times F_S \times F_E \quad (30)$$

$$\overline{W} = \left[\sum_{t'=1}^k W \right]^{-1} W \quad (31)$$

where W refers to the aggregated weight map and F_C , F_E , and F_S represents the feature weight of contrast, exposure, and saturation, respectively. \overline{W} denotes the normalized aggregated weight map, and k represents the number of input images.

2) *Fusion*: MF is used to fuse the weight map and the input map pixel by pixel using a multiscale strategy based on Laplacian and Gaussian pyramids. The Gaussian pyramid filters the input image with a lowpass Gaussian kernel at each layer and then decomposes the image into the sum of the bandpass images. After multiscale decomposition is complete, the pyramids of the decomposed input map and weight map are at a uniform level, and the maps are fused pixel by pixel and reconstructed

into a final image. The equation is as follows:

$$R_l(x) = \sum_{t=1}^k G_l\{\bar{W}_t\}L_l\{I\} \quad (32)$$

where $R_l(x)$ represents the reconstructed result image, $G_l\{\bar{W}_t\}$ denotes the Gaussian pyramid decomposed from the weight map, and $L_l\{I\}$ represents the Laplacian pyramid decomposed from the input image.

IV. EVALUATION AND DISCUSSION

The underwater image quality obtained by the proposed method is evaluated using a qualitative evaluation, quantitative evaluation, an ablation experiment, and a runtime evaluation. The qualitative evaluation uses instruments to observe or perform repeated observation experiments on the image. Then, multiple testers evaluate and analyze the quality of the image. The quantitative evaluation calculates the objective evaluation index of the image using mathematical methods and determines the image's quality using the results of these calculations. In this study, ten representative methods are selected and compared with the proposed method. These methods consist of four enhancement methods, four restoration methods, and two deep learning methods. They include single image haze removal using DCP [27], transmission estimation in single underwater images (UDCP) [28], underwater image restoration based on IBLA [29], and an underwater scene rapid depth estimation model based on the underwater light attenuation prior (ULAP) [31].

An integrated color model (ICM) for underwater image processing [32], a multiscale correlated wavelet approach (WB) [36], a TS method for single underwater imaging process improvement [33], shallow-water image improvement using RGHS based on adaptive parameter acquisition [34], underwater image and video enhancement with a CNN model (UWCNN) [46], and an underwater imaging improvement network called Water-Net (WNT) [43] are used. The data set used in this paper includes an underwater image enhancement benchmark (UIEB) database [43] and the data set provided by the Zhangzidao Laboratory of Dalian University of Technology. The UIEB database consists of 950 real-world underwater images, with 60 images that can be used as challenging data because satisfactory reference images cannot be obtained. Furthermore, the original underwater images in UIEB were taken under natural light, artificial light, or a mixture of the two; therefore, the images' color range and contrast reduction are different. The Zhangzidao data set includes images of sea urchins and scallops collected by the Zhangzidao Laboratory of the Dalian University of Technology using underwater robots in Zhangzidao, Dalian.

The UIEB data set is divided into two main scenarios: greenish and blueish. The greenish images are called data A, whereas the blueish images are called data B. The Zhangzidao data set is called data C for comparative analysis.

A. Qualitative Evaluation

Data A, B, and C are used for qualitative evaluation. Ten comparison methods are selected for comparative analysis for data A

and B. Eight representative images are shown in Fig. 6. To better test the performance of the proposed method in real underwater scenes, data C is used for further quantitative evaluation, and eight representative images are shown in Fig. 7.

Although DCP removes the haze in the original underwater image, it fails to achieve good visibility, color, and detail results. UDCP only employs the BG channels to estimate the transmission image; thus, it does not affect some underwater images and aggravates the color cast of the images. Although IBLA considers the effects of scattering and absorption, it does not consider color compensation, which causes red artifacts in some underwater images. Due to ULAP's poor improvement in the RB channels, the entire output image is covered in shades of green. Additionally, the inaccuracy of the physical model and the assumptions used in the method make the elimination of the backscatter effects impossible. Although ICM redistributes the S and I components in the HSI color space and increases the image contrast to a certain extent, the method cannot enhance the dark areas and instead produces oversaturated areas. The TS method cannot accurately select the target image when processing the contrast improvement, which leads to only a slight increase in the contrast of the images. Furthermore, the images still have some problems with dark color and brightness. Because WB cannot reveal the characteristics of the scene, it cannot change the overall tone of the image. Although the visibility of the image is slightly improved, the result is still unsatisfactory. Although the RGHS method effectively improves the image's contrast, it ignores the relationship between the underwater image degradation and the field depth. Therefore, some of the results still have color cast problems. The model and network structure of UWCNN are unsuitable for some images, resulting in poor color cast, visibility, and contrast. Water-Net uses the resulting image processed by the traditional methods as the input image and ignores the influence of the imaging model, which limits the method's performance.

In contrast, the proposed approach solves the color cast and improves color saturation using the SLVC algorithm. Additionally, it solves the low contrast and detail problems using the MSHE algorithm. Thus, the quantitative evaluation demonstrates that the proposed method achieves a better visual effect than the other reported methods.

B. Quantitative Evaluation

A quantitative evaluation is used to calculate the objective index value, and thus, the images' contrast, color, and visibility are evaluated. The metrics include the average gradient (AG) [52], IE [52], the patch-based contrast quality index (PCQI), natural image quality evaluator (NIQE) [44], structural similarity (SSIM) [10], underwater image colorfulness measure (UICM) [52], underwater image quality metric (UIQM) [52], and underwater color image quality evaluation (UCIQE) [53]. AG represents the image visibility, IE represents the richness of the image information, PCQI represents the image clarity, SSIM represents the richness of the recovered salient information of the image, UICM represents the color quality of underwater images, UIQM measures the balance of color, contrast, and sharpness, and

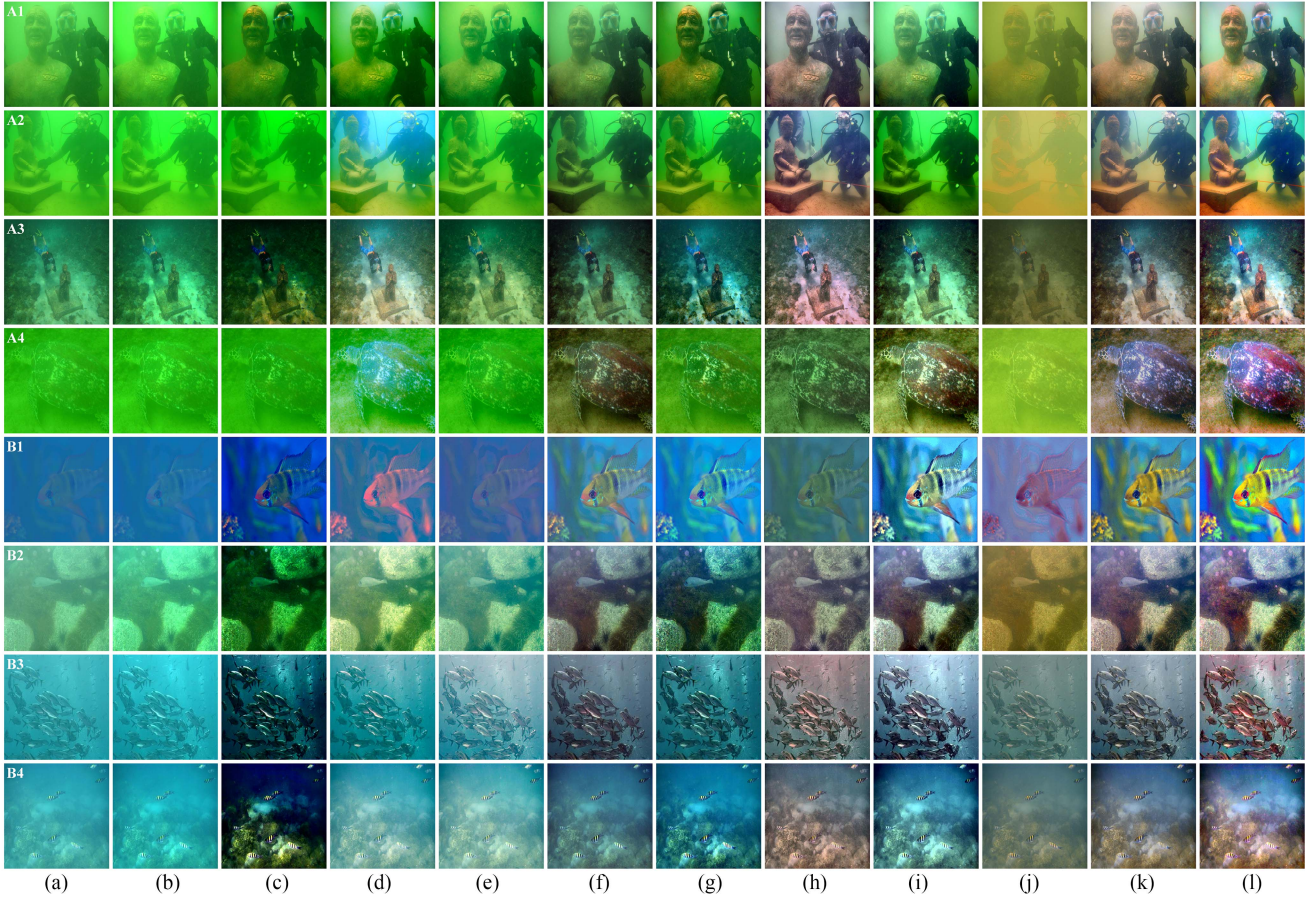


Fig. 6. Quantitative comparison of data A and data B. From left to right: raw underwater images, DCP [27], UDCP [28], IBLA [29], ULAP [31], ICM [32], WB [36], TS [33], RGHS [34], UWCNN [46], WNT [43], and our method.

TABLE I
AVERAGE VALUES OF THE OBJECTIVE METRICS SSIM, PCQI, NIQE, AND UIQM METRICS ON IMAGES FROM DATA A AND DATA B

	DCP	UDCP	IBLA	ULAP	ICM	WB	TS	RGHS	UWCNN	WNT	Ours
SSIM	0.625	0.493	0.665	0.539	0.701	0.648	0.745	0.747	0.472	0.807	0.752
PCQI	0.927	0.796	1.012	1.031	0.997	0.972	1.113	1.047	0.776	0.977	1.058
NIQE	4.510	4.274	4.161	4.291	4.343	4.361	4.050	4.086	4.481	4.184	4.240
UIQM	1.020	1.448	1.162	1.158	1.164	1.277	1.269	1.301	0.903	1.202	1.290

The best value is marked in red bold, and the second value is marked in blue bold.

UCIQE measures the balance of chroma, saturation, and contrast. The lower the NIQE score is the better the image quality.

A quantitative evaluation is performed on the images of data A and data B. For the UIEB data set, eight representative images (four each data A and data B) are selected to calculate the objective index value, which is illustrated by line charts. Then, the average value of the objective index is calculated for the results obtained by the different methods; this is illustrated by the bar graphs (see Fig. 8). Furthermore, the average value of some objective index is calculated in Table I, which covers all comparison methods and 114 representative severely degraded images in the data set A and B. In addition, the UICM values of eight representative images are shown in Table II.

UDCP, IBLA, ULAP, and WB do not address the problem of color casting in the images, which results in higher IE values,

while the UCIQE and AG values are more typical than IE. ICM increases the image contrast to a certain extent, so the UCIQE value increases, but this method cannot enhance the dark area. The average UCIQE of RGHS is close to the proposed method, but its color correction effect still needs to be improved. Since TS obtains more image details, the average AG of TS is higher than the proposed method, but TS also increases the noise of the image. DCP and UWCNN have poor UCIQE, AG, and IE values and the worst recovery effect, and the image quality still needs improvement. The TS and WNT methods improve the contrast, chroma, and saturation of the image, but the effect can still be improved. Furthermore, the SSIM values of the proposed method are only lower than those of WNT. The PCQI values of the proposed method are lower than those of TS, but TS is poor at removing the color cast and improving contrast. The NIQE

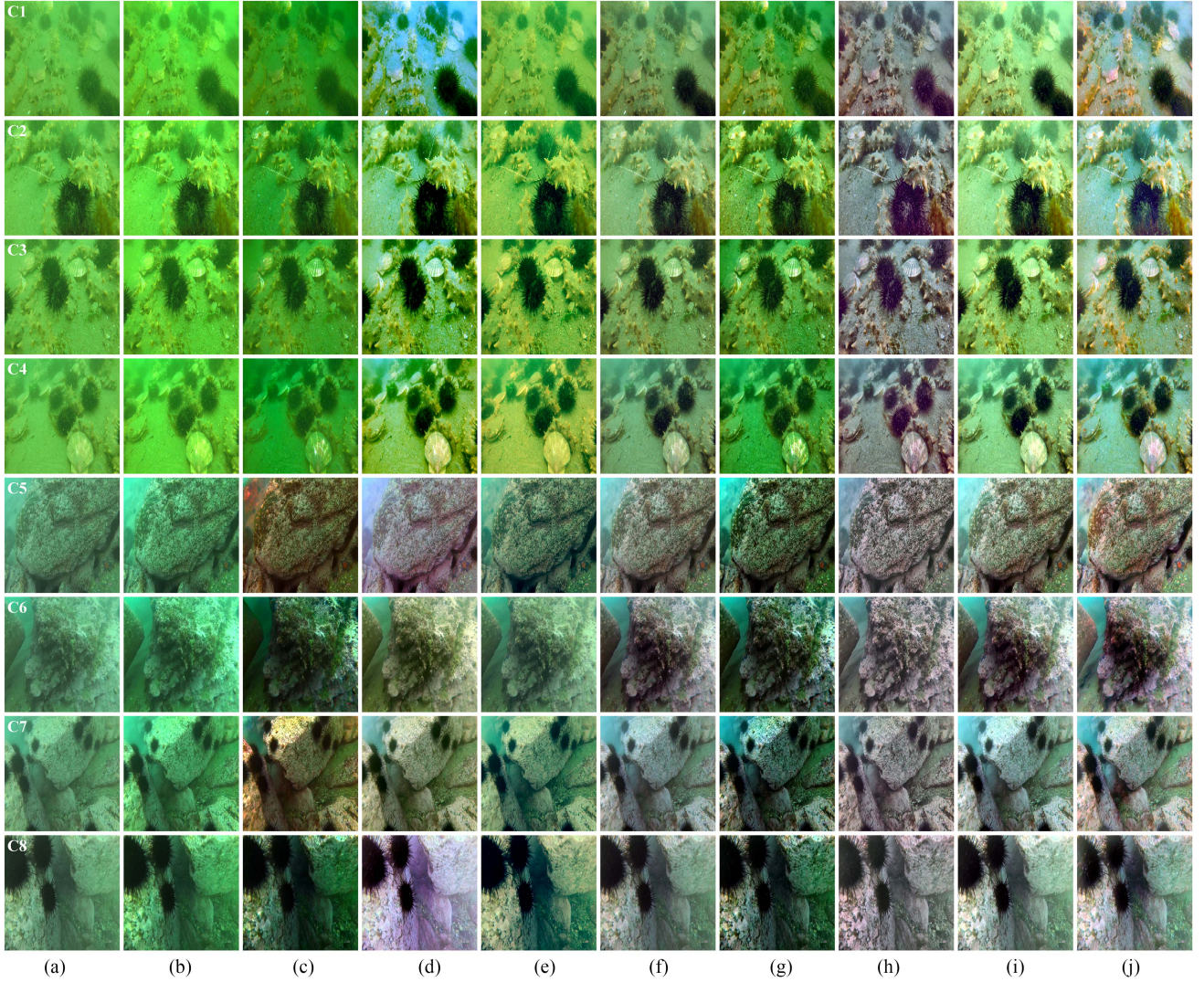


Fig. 7. Quantitative comparison of data C. From left to right: raw underwater images, DCP [27], UDCP [28], IBLA [29], ULAP [31], ICM [32], WB [36], TS [33], RGHS [34], and our method.

TABLE II
COMPARISON OF THE OBJECTIVE UICM METRICS ON REPRESENTATIVE IMAGES FROM DATA A AND DATA B

	DCP	UDCP	IBLA	ULAP	ICM	WB	TS	RGHS	UWCNN	WNT	Ours
A1	-0.59	1.16	1.99	1.59	2.46	2.40	3.03	2.95	-0.06	2.63	5.19
A2	-1.01	-0.27	9.47	1.04	3.16	3.16	7.31	3.83	-0.26	6.56	11.76
A3	0.09	1.59	3.33	1.54	2.28	2.28	4.48	2.87	0.46	3.13	5.93
A4	-3.48	-3.15	2.57	-2.70	1.37	1.37	0.26	2.04	-2.51	4.19	6.59
B1	-1.81	0.80	4.28	-0.08	3.00	3.00	0.47	3.29	2.06	7.54	10.80
B2	-0.57	1.99	1.47	1.24	2.56	2.56	1.84	3.65	-0.16	3.46	4.99
B3	-2.66	2.33	-0.71	1.59	0.67	0.67	2.25	0.94	0.12	0.53	3.79
B4	-1.41	4.14	2.01	1.80	1.11	1.11	3.76	1.25	1.66	4.07	6.48

The best value is marked in red bold.

values of the proposed method are higher than IBLA, TS, RGSH, and WNT. However, these methods all have obvious degradation problems that have not been solved. The UIQM value of the proposed method is lower than that of RGHS and UDCP, but none can solve the image with a serious color cast. In addition,

it can be seen that the UICM value of the resulting image of the proposed method is better than that of the other methods, demonstrating that the proposed method has better color quality. The UCIQE, AG, IE, UICM, PCQI, NIQE, and UIQM values of the proposed method are superior to those of some advanced

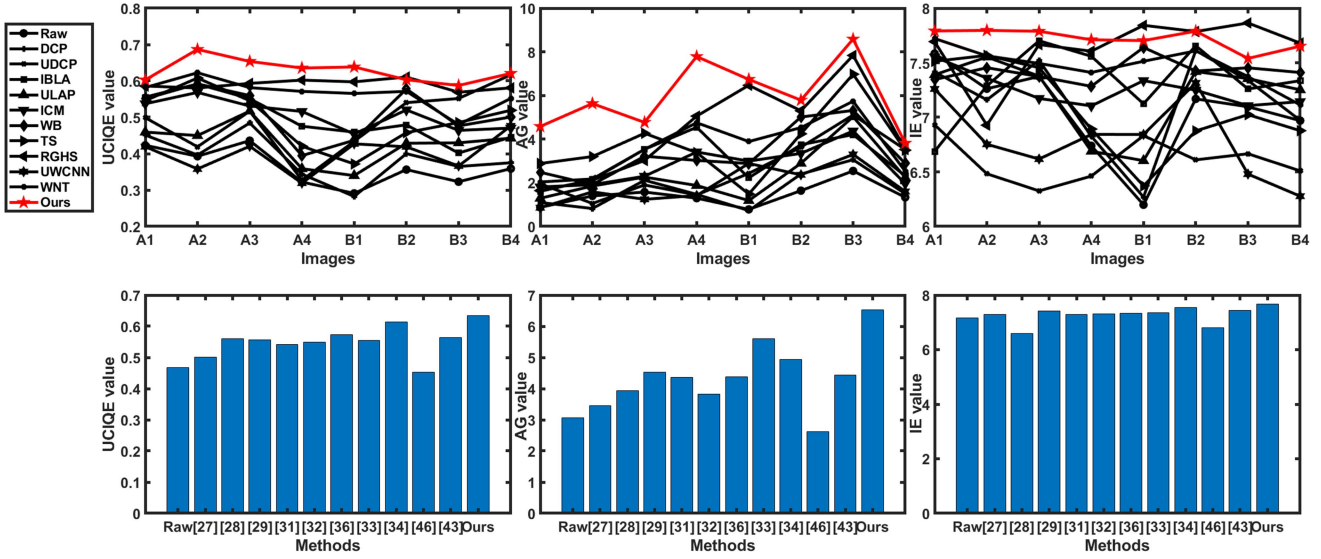


Fig. 8. Comparison of the objective indicators of data A and B. (a)–(c) Line graphs of the objective index values of the representative images. (d)–(f) Bar graphs based on the average objective index value calculated from all images in the data set. From left to right, the abscissas are the raw images, DCP [27], UDCP [28], IBLA [29], ULAP [31], ICM [32], WB [36], TS [33], RGHS [34], UWCNN [46], WNT [43], and ours.

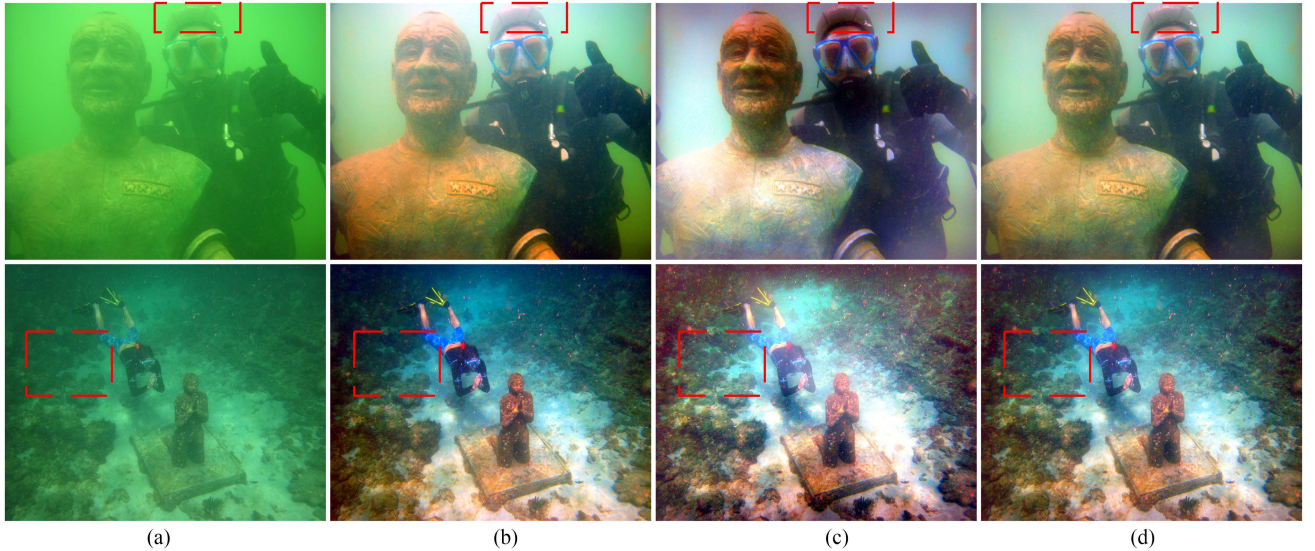


Fig. 9. Schematic diagram of the ablation experiments on the representative underwater images. From left to right are (a) raw image and the resulting images of (b) SLVC, (c) MSHE, and (d) UMSHE.

methods, demonstrating that our method can better adjust the chroma, saturation, and contrast of images, making the images clearer and richer in color information than those rendered by the other methods.

C. Ablation Experiment

To better illustrate the effectiveness and rationality of each part, an ablation experiment is designed to evaluate each part. Fig. 9 lists the subjective results of some representative underwater images applied to each part. The results demonstrate that the SLVC method can better remove the color cast, but there is a problem with missing details. The MSHE method

can improve the image contrast to obtain more details, but there are problems with poor color quality and overexposure. After the resulting images of the SLVC method and the MSHE method are fused by the MF method, the result not only has higher color quality; but also has more image details and higher contrast.

The subjective evaluation shows that the proposed method has better visual effects. In addition, eight representative images in data set C are selected to calculate the UIQM values of the result images processed by the proposed method and its submethods, respectively. To better illustrate the effect of the ablation experiment, we also selected 300 images in data set C to obtain their average UIQM values, which are listed in

TABLE III
COMPARISON OF THE UIQM VALUES OF SUBMETHOD OF THE METHOD

	C1	C2	C3	C4	C5	C6	C7	C8	AVG
Raw	0.812	0.778	1.536	1.492	1.443	0.590	0.710	1.038	0.876
SLVC	1.431	1.401	1.562	1.549	1.527	1.239	1.239	1.494	1.337
MSHE	1.447	1.299	1.523	1.559	1.403	1.242	1.108	1.402	1.278
UMSHE	1.449	1.422	1.573	1.570	1.556	1.247	1.245	1.503	1.369

The best value is marked in red bold

TABLE IV
RUNTIME OF DIFFERENT METHODS FOR PROCESSING DIFFERENT RESOLUTION RATIO IMAGES

Methods	256 * 256	640 * 480	1024 * 768	1920 * 1082
DCP	0.29 s	0.87 s	1.87 s	4.96 s
UDCP	0.85 s	3.11 s	7.82 s	20.89 s
IBLA	11.66 s	36.73 s	114.32 s	1171.38 s
ULAP	0.54 s	2.21 s	5.12 s	12.94 s
ICM	0.85 s	4.03 s	9.61 s	26.36 s
WB	0.68 s	1.01 s	1.86 s	3.92 s
TS	0.11 s	0.46 s	1.29 s	3.06 s
RGHS	1.11 s	4.95 s	12.88 s	33.65 s
Our method	0.36 s	2.91 s	6.09 s	16.65 s

Table III. The objective results show that the final proposed method has a better balance of color, contrast, and sharpness than the submethod. Therefore, the ablation experiment demonstrates that each part of our method is effective and reasonable, and the proposed method has an excellent subjective and objective evaluation performance.

D. Runtime Evaluation

Various comparison methods, including DCP, UDCP, IBLA, ULAP, ICM, WB, TS, and RGHS, are selected for runtime evaluation. The runtime of different methods for processing images of different sizes is shown in Table IV, and the unit of the running time is seconds (s). The results show that the performance of the runtime of the proposed method is not the best. However, it is still faster than some advanced methods, such as UDCP, IBLA, ICM, and RGHS.

V. CONCLUSION

This work estimates the degree of feature drift of different areas of an image by the statistical characteristics of the image. The information is adopted to guide feature enhancement and then improve the visual effect of the degraded image. Based on this, the characteristics of underwater image histograms are estimated, and a novel underwater image improvement method with color correction and MSHE is proposed. SLVC is designed to address the color cast and enhance the saturation. By adding the variational model for processing, the performance of removing the color cast and enhancing the saturation is better and more reasonable. The MSHE method is employed to improve the contrast and details of the image. Reasonable thresholds are chosen to divide multiple histograms and equalize them separately, obtaining detailed information and improving the

contrast. Finally, MF is adopted to fuse the resulting images and obtain the final enhanced image. The qualitative and quantitative results show that the technique successfully resolves images' color cast and improves the saturation, contrast, and detail information. Through our research, SHE is extended from a fixed number to any number, and the performance and adaptability of SHE are further improved. This paper shows that a moderate increase in subhistograms and a more precise division threshold selection can improve HE performance. Based on the excellent performance of our method, the proposed method can be further studied and extended in high-level underwater tasks.

However, our method still has shortcomings. First, the method may produce red shading for some deep-sea images. In addition, this method does not consider the effect of different underwater scenes and scene depths. For the red shading, we will increase the division of the image area and the judgment of whether the pixel value needs to be adjusted and selectively enhance the area of the image to avoid repeated adjustment of image pixels. For the underwater scenes and depths, we will use the scene depth as a parameter in the formula of MSHE and select data sets of different scenes for further study. We will optimize our method to adaptively adjust the enhancement levels according to light and depth changes.

REFERENCES

- [1] Z. Jiang, Z. Li, S. Yang, X. Fan, and R. Liu, "Target oriented perceptual adversarial fusion network for underwater image enhancement," *IEEE Trans. Circuits Syst. Video Technol.*, vol. 32, no. 10, pp. 6584–6598, Oct. 2022, doi: [10.1109/TCSVT.2022.3174817](https://doi.org/10.1109/TCSVT.2022.3174817).
- [2] P. Zhuang, C. Li, and J. Wu, "Bayesian retinex underwater image enhancement," *Eng. Appl. Artif. Intell.*, vol. 101, 2021, Art. no. 104171, doi: [10.1016/j.engappai.2021.104171](https://doi.org/10.1016/j.engappai.2021.104171).
- [3] R. Liu, Z. Jiang, S. Yang, and X. Fan, "Twin adversarial contrastive learning for underwater image enhancement and beyond," *IEEE Trans. Image Process.*, vol. 31, pp. 4922–4936, 2022, doi: [10.1109/TIP.2022.3190209](https://doi.org/10.1109/TIP.2022.3190209).

- [4] W. Ren, J. Pan, H. Zhang, X. Cao, and M. H. Yang, "Single image dehazing via multi-scale convolutional neural networks with holistic edges," *Int. J. Comput. Vis.*, vol. 128, no. 1, pp. 240–259, 2020, doi: [10.1007/s11263-019-01235-8](https://doi.org/10.1007/s11263-019-01235-8).
- [5] S. Anwar and C. Li, "Diving deeper into underwater image enhancement: A survey," *Signal Process., Image Commun.*, vol. 89, Nov. 2020, Art. no. 115978, doi: [10.1016/j.image.2020.115978](https://doi.org/10.1016/j.image.2020.115978).
- [6] J. Zhou, T. Yang, W. Ren, D. Zhang, and W. Zhang, "Underwater image restoration via depth map and illumination estimation based on single image," *Opt. Exp.*, vol. 29, no. 19, pp. 29864–29886, 2021, doi: [10.1364/OE.427839](https://doi.org/10.1364/OE.427839).
- [7] C. Li, S. Anwar, J. Hou, R. Cong, C. Guo, and W. Ren, "Underwater image enhancement via medium transmission-guided multi-color space embedding," *IEEE Trans. Image Process.*, vol. 30, pp. 4985–5000, 2021, doi: [10.1109/TIP.2021.3076367](https://doi.org/10.1109/TIP.2021.3076367).
- [8] J. Zhou, T. Yang, and W. Zhang, "Underwater vision enhancement technologies: A comprehensive review, challenges, and recent trends," *Appl. Intell.*, vol. 52, pp. 1–28, 2022, doi: [10.1007/s10489-022-03767-y](https://doi.org/10.1007/s10489-022-03767-y).
- [9] T. Li, Q. Yang, S. Rong, L. Chen, and B. He, "Distorted underwater image reconstruction for an autonomous underwater vehicle based on a self-attention generative adversarial network," *Appl. Opt.*, vol. 59, no. 32, pp. 10049–10060, 2020, doi: [10.1364/AO.402024](https://doi.org/10.1364/AO.402024).
- [10] X. Ding, Z. Liang, Y. Wang, and X. Fu, "Depth-aware total variation regularization for underwater image dehazing," *Signal Process., Image Commun.*, vol. 98, 2021, Art. no. 116408, doi: [10.1016/j.image.2021.116408](https://doi.org/10.1016/j.image.2021.116408).
- [11] T. Li et al., "Underwater image enhancement framework using adaptive color restoration and dehazing," *Opt. Express*, vol. 30, no. 4, pp. 6216–6235, 2022, doi: [10.1364/OE.449930](https://doi.org/10.1364/OE.449930).
- [12] J. Zhou, D. Zhang, W. Ren, and W. Zhang, "Auto color correction of underwater images utilizing depth information," *IEEE Geosci. Remote Sens. Lett.*, vol. 19, 2022, Art. no. 1504805, doi: [10.1109/LGRS.2022.3170702](https://doi.org/10.1109/LGRS.2022.3170702).
- [13] J. Zhou, T. Yang, W. Chu, and W. Zhang, "Underwater image restoration via backscatter pixel prior and color compensation," *Eng. Appl. Artif. Intell.*, vol. 111, 2022, Art. no. 104785, doi: [10.1016/j.engappai.2022.104785](https://doi.org/10.1016/j.engappai.2022.104785).
- [14] P. Zhuang, J. Wu, F. Porikli, and C. Li, "Underwater image enhancement with hyper-laplacian reflectance priors," *IEEE Trans. Image Process.*, vol. 31, pp. 5442–5455, 2022, doi: [10.1109/TIP.2022.3196546](https://doi.org/10.1109/TIP.2022.3196546).
- [15] J. Zhou, D. Zhang, and W. Zhang, "Classical and state-of-the-art approaches for underwater image defogging: A comprehensive survey," *Front. Inf. Technol. Electron. Eng.*, vol. 21, no. 5, pp. 1745–1769, 2020, doi: [10.1631/FITEE.2000190](https://doi.org/10.1631/FITEE.2000190).
- [16] Y. Guo, H. Li, and P. Zhuang, "Underwater image enhancement using a multiscale dense generative adversarial network," *IEEE J. Ocean. Eng.*, vol. 45, no. 3, pp. 862–870, Jul. 2020, doi: [10.1109/JOE.2019.2911447](https://doi.org/10.1109/JOE.2019.2911447).
- [17] Y.-T. Kim, "Contrast enhancement using brightness preserving bi-histogram equalization," *IEEE Trans. Consum. Electron.*, vol. 43, no. 1, pp. 1–8, Feb. 1997, doi: [10.1109/30.580378](https://doi.org/10.1109/30.580378).
- [18] Y. Wang, Q. Chen, and B. Zhang, "Image enhancement based on equal area dualistic sub-image histogram equalization method," *IEEE Trans. Consum. Electron.*, vol. 45, no. 1, pp. 68–75, Feb. 1999, doi: [10.1109/30.754419](https://doi.org/10.1109/30.754419).
- [19] M. F. Khan, D. Goyal, M. M. Nofal, E. Khan, R. Al-Hmouz, and E. Herrera-Viedma, "Fuzzy-based histogram partitioning for bi-histogram equalization of low contrast images," *IEEE Access*, vol. 8, pp. 11595–11614, 2020, doi: [10.1109/ACCESS.2020.2965174](https://doi.org/10.1109/ACCESS.2020.2965174).
- [20] H.-H. Chang, C.-Y. Cheng, and C.-C. Sung, "Single underwater image restoration based on depth estimation and transmission compensation," *IEEE J. Ocean. Eng.*, vol. 44, no. 4, pp. 1130–1149, Oct. 2019, doi: [10.1109/JOE.2018.2865045](https://doi.org/10.1109/JOE.2018.2865045).
- [21] T. Treibitz and Y. Y. Schechner, "Active polarization descattering," *IEEE Trans. Pattern Anal. Mach. Intell.*, vol. 31, no. 3, pp. 385–399, Mar. 2009, doi: [10.1109/TPAMI.2008.85](https://doi.org/10.1109/TPAMI.2008.85).
- [22] Z. Chen, H. Wang, J. Shen, X. Li, and L. Xu, "Region-specialized underwater image restoration in inhomogeneous optical environments," *Optik*, vol. 125, no. 9, pp. 2090–2098, May 2014, doi: [10.1016/j.jleo.2013.10.038](https://doi.org/10.1016/j.jleo.2013.10.038).
- [23] H. Hu, L. Zhao, B. Huang, X. Li, H. Wang, and T. Liu, "Enhancing visibility of polarimetric underwater image by transmittance correction," *IEEE Photon. J.*, vol. 9, no. 3, Jun. 2017, Art. no. 6802310, doi: [10.1109/JPHOT.2017.2698000](https://doi.org/10.1109/JPHOT.2017.2698000).
- [24] E. Trucco and A. T. Olmos-Antillon, "Self-tuning underwater image restoration," *IEEE J. Ocean. Eng.*, vol. 31, no. 2, pp. 511–519, Apr. 2006, doi: [10.1109/JOE.2004.836395](https://doi.org/10.1109/JOE.2004.836395).
- [25] W. Hou, D. J. Gray, A. D. Weidemann, G. R. Fournier, and J. L. Forand, "Automated underwater image restoration and retrieval of related optical properties," in *Proc. IEEE Int. Geosci. Remote Sens. Symp.*, 2007, pp. 1889–1892, doi: [10.1109/IGARSS.2007.4423193](https://doi.org/10.1109/IGARSS.2007.4423193).
- [26] M. Boffety, F. Galland, and A. G. Allais, "Color image simulation for underwater optics," *Appl. Opt.*, vol. 51, no. 23, pp. 5633–5642, 2012, doi: [10.1364/AO.51.005633](https://doi.org/10.1364/AO.51.005633).
- [27] K. He, J. Sun, and X. Tang, "Single image haze removal using dark channel prior," *IEEE Trans. Pattern Anal. Mach. Intell.*, vol. 33, no. 12, pp. 2341–2353, Dec. 2011, doi: [10.1109/TPAMI.2010.168](https://doi.org/10.1109/TPAMI.2010.168).
- [28] P. Drews, E. Nascimento, F. Moraes, S. Botelho, and M. Campos, "Transmission estimation in underwater single images," in *Proc. IEEE Int. Conf. Comput. Vis. Workshops*, 2013, pp. 825–830, doi: [10.1109/ICCVW.2013.113](https://doi.org/10.1109/ICCVW.2013.113).
- [29] Y.-T. Peng and P. C. Cosman, "Underwater image restoration based on image blurriness and light absorption," *IEEE Trans. Image Process.*, vol. 26, no. 4, pp. 1579–1594, Apr. 2017, doi: [10.1109/TIP.2017.2663846](https://doi.org/10.1109/TIP.2017.2663846).
- [30] C.-Y. Li, J.-C. Guo, R.-M. Cong, Y.-W. Pang, and B. Wang, "Underwater image enhancement by dehazing with minimum information loss and histogram distribution prior," *IEEE Trans. Image Process.*, vol. 25, no. 12, pp. 5664–5677, Dec. 2016, doi: [10.1109/TIP.2016.2612882](https://doi.org/10.1109/TIP.2016.2612882).
- [31] W. Song, Y. Wang, D. Huang, and D. Tjomdronegoro, "A rapid scene depth estimation model based on underwater light attenuation prior for underwater image restoration," *Pac. Rim Conf. Multimedia*, vol. 11164, pp. 678–688, 2018, doi: [10.1007/978-3-030-00776-8_62](https://doi.org/10.1007/978-3-030-00776-8_62).
- [32] K. Iqbal, R. A. Salam, A. Osman, and A. Z. Talib, "Underwater image enhancement using an integrated color model," *IAENG Int. J. Comput. Sci.*, vol. 34, no. 2, p. 12, 2007.
- [33] X. Fu, Z. Fan, M. Ling, Y. Huang, and X. Ding, "Two-step approach for single underwater image enhancement," in *Proc. Int. Symp. Intell. Signal Process. Commun. Syst.*, 2017, pp. 789–794, doi: [10.1109/IS-PACS.2017.8266583](https://doi.org/10.1109/IS-PACS.2017.8266583).
- [34] D. Huang, Y. Wang, W. Song, J. Sequeira, and S. Mavromatis, "Shallow-water image enhancement using relative global histogram stretching based on adaptive parameter acquisition," in *Proc. Int. Conf. Multimedia Model.*, 2018, pp. 453–465, doi: [10.1007/978-3-319-73603-7_37](https://doi.org/10.1007/978-3-319-73603-7_37).
- [35] A. Khan, A. S. Ali, A. S. Malik, A. Anwer, and F. Meriaudeau, "Underwater image enhancement by wavelet-based fusion," in *Proc. IEEE Int. Conf. Underwater Syst. Technol., Theory Appl.*, 2016, pp. 83–88, doi: [10.1109/USYS.2016.7893927](https://doi.org/10.1109/USYS.2016.7893927).
- [36] X. Liu, H. Zhang, Y. Cheung, X. You, and Y. Tang, "Efficient single image dehazing and denoising: An efficient multi-scale correlated wavelet approach," *Comput. Vis. Image Understanding*, vol. 162, pp. 23–33, Sep. 2017, doi: [10.1016/j.cviu.2017.08.002](https://doi.org/10.1016/j.cviu.2017.08.002).
- [37] S. Vasamsetti, N. Mittal, B. C. Neelapu, and H. K. Sardana, "Wavelet based perspective on variational enhancement technique for underwater imagery," *Ocean Eng.*, vol. 141, pp. 88–100, Sep. 2017, doi: [10.1016/j.oceaneng.2017.06.012](https://doi.org/10.1016/j.oceaneng.2017.06.012).
- [38] C. Ancuti, C. O. Ancuti, T. Haber, and P. Bekaert, "Enhancing underwater images and videos by fusion," in *Proc. IEEE Conf. Comput. Vis. Pattern Recognit.*, 2012, pp. 81–88, doi: [10.1109/CVPR.2012.6247661](https://doi.org/10.1109/CVPR.2012.6247661).
- [39] C. O. Ancuti, C. De Vleeschouwer, and P. Bekaert, "Color balance and fusion for underwater image enhancement," *IEEE Trans. Image Process.*, vol. 27, no. 1, pp. 379–393, Jan. 2018, doi: [10.1109/TIP.2017.2759252](https://doi.org/10.1109/TIP.2017.2759252).
- [40] H. Lu, Y. Li, L. Zhang, and S. Serikawa, "Contrast enhancement for images in turbid water," *J. Opt. Soc. Amer. A*, vol. 32, no. 5, pp. 886–893, doi: [10.1364/JOSAA.32.000886](https://doi.org/10.1364/JOSAA.32.000886).
- [41] C. Li, J. Guo, and C. Guo, "Emerging from water: Underwater image color correction based on weakly supervised color transfer," *IEEE Signal Process. Lett.*, vol. 25, no. 3, pp. 323–327, Mar. 2018, doi: [10.1109/LSP.2018.2792050](https://doi.org/10.1109/LSP.2018.2792050).
- [42] I. Goodfellow et al., "Generative adversarial networks," *Commun. ACM*, vol. 63, no. 11, pp. 139–144, 2020, doi: [10.1145/3422622](https://doi.org/10.1145/3422622).
- [43] C. Li et al., "An underwater image enhancement benchmark dataset and beyond," *IEEE Trans. Image Process.*, vol. 29, pp. 4376–4389, 2020, doi: [10.1109/TIP.2019.2955241](https://doi.org/10.1109/TIP.2019.2955241).
- [44] H. Li, J. Li, and W. Wang, "A fusion adversarial underwater image enhancement network with a public test dataset," 2019, *arXiv:1906.06819*.
- [45] K. Cao, Y.-T. Peng, and P. C. Cosman, "Underwater image restoration using deep networks to estimate background light and scene depth," in *Proc. IEEE Southwest Symp. Image Anal. Interpretation*, 2018, pp. 1–4, doi: [10.1109/SSIAI.2018.8470347](https://doi.org/10.1109/SSIAI.2018.8470347).

- [46] C. Li and S. Anwar, "Underwater scene prior inspired deep underwater image and video enhancement," *Pattern Recognit.*, vol. 98, no. 1, Feb. 2020, Art. no. 107038, doi: [10.1016/j.patcog.2019.107038](https://doi.org/10.1016/j.patcog.2019.107038).
- [47] W. Zhang, L. Dong, T. Zhang, and W. Xu, "Enhancing underwater image via color correction and bi-interval contrast enhancement," *Signal Process., Image Commun.*, vol. 90, Jan. 2021, Art. no. 116030, doi: [10.1016/j.image.2020.116030](https://doi.org/10.1016/j.image.2020.116030).
- [48] M. Bertalmio, V. Caselles, E. Provenzi, and A. Rizzi, "Perceptual color correction through variational techniques," *IEEE Trans. Image Process.*, vol. 16, no. 4, pp. 1058–1072, Apr. 2007, doi: [10.1109/TIP.2007.891777](https://doi.org/10.1109/TIP.2007.891777).
- [49] X. Li, G. Hou, L. Tan, and W. Liu, "A hybrid framework for underwater image enhancement," *IEEE Access*, vol. 8, pp. 197448–197462, 2020, doi: [10.1109/ACCESS.2020.3034275](https://doi.org/10.1109/ACCESS.2020.3034275).
- [50] C. Ding, X. Pan, X. Gao, L. Ning, and Z. Wu, "Three adaptive sub-histograms equalization algorithm for maritime image enhancement," *IEEE Access*, vol. 8, pp. 147983–147994, 2020, doi: [10.1109/ACCESS.2020.3015839](https://doi.org/10.1109/ACCESS.2020.3015839).
- [51] C. O. Ancuti and C. Ancuti, "Single image dehazing by multi-scale fusion," *IEEE Trans. Image Process.*, vol. 22, no. 8, pp. 3271–3282, Aug. 2013, doi: [10.1109/TIP.2013.2262284](https://doi.org/10.1109/TIP.2013.2262284).
- [52] M. Han, Z. Lyu, T. Qiu, and M. Xu, "A review on intelligence dehazing and color restoration for underwater images," *IEEE Trans. Syst.*, vol. 50, no. 5, pp. 1820–1832, May 2020, doi: [10.1109/TSMC.2017.2788902](https://doi.org/10.1109/TSMC.2017.2788902).
- [53] M. Yang and A. Sowmya, "An underwater color image quality evaluation metric," *IEEE Trans. Image Process.*, vol. 24, no. 12, pp. 6062–6071, Dec. 2015, doi: [10.1109/TIP.2015.2491020](https://doi.org/10.1109/TIP.2015.2491020).



Jingchun Zhou received the M.S. degrees in software engineering from the Beijing University of Posts and Telecommunications, Beijing, China, in 2016, and computer information technology from Northern Arizona University, Flagstaff, AZ, USA, in 2022, and the Ph.D. degree in computer applications from Dalian Maritime University, Dalian, China, in 2021.

He is currently a Postdoctoral Researcher with Dalian Maritime University. His research interests include computer vision, deep learning, and underwater image enhancement.

Dr. Zhou is a reviewer for IEEE TRANSACTIONS ON IMAGE PROCESSING, IEEE TRANSACTIONS ON GEOSCIENCE AND REMOTE SENSING, IEEE SIGNAL PROCESSING LETTERS, IEEE JOURNAL OF OCEANIC ENGINEERING, Artificial Intelligence, Engineering Applications of Artificial Intelligence, Information Fusion, Applied Mathematical Modeling, Computers and Electronics in Agriculture, Computers and Electrical Engineering, Signal Processing Image Communication, Neurocomputing, Optics Express, Asian Conference on Computer Vision, etc.



Lei Pang received the B.S. degree in software engineering from Liaoning Technical University, Fuxin, China, in 2020. He is currently working toward the M.S. degree in software engineering with Dalian Maritime University, Dalian, China, in 1996.

His main research interests include computer vision, image enhancement and defogging, and target recognition.



Dehuan Zhang received the M.S. degree in computer science and technology from Dalian Maritime University, Dalian, China, in 2021, where she is currently working toward the Ph.D. degree in computer science and technology.

Her research interests include computer vision, deep learning, and image processing.



Weishi Zhang received the B.S. degree in computer science from Xi'an Jiaotong University, China, in 1984, and the M.S. degree in computer science from Chinese Academy of Science, China, in 1986, and the Ph.D. degree in computer science from University of Munich, Germany, in 1996.

He is currently a Professor with the College of Information Science and Technology, Dalian Maritime University, Dalian, China. His research interests include computer vision, pattern recognition, software engineering, and software architecture.